Citation
Fatima, H. and Azhar, M.R. and Zhong, Y. and Arafat, Y. and Khiadani, M. and Shao, Z. 2022. Rational design of ZnO-zeolite imidazole hybrid nanoparticles with reduced charge recombination for enhanced photocatalysis. Journal of Colloid and Interface Science. 614: pp. 538-546. http://doi.org/10.1016/j.jcis.2022.01.086

Rational design of ZnO-zeolite imidazole hybrid nanoparticles with reduced charge recombination for enhanced photocatalysis

Hira Fatima[1], Muhammad Rizwan Azhar[2], Yijun Zhong*[,1], Yasir Arafat[1], Mehdi Khiadani[2], Zongping Shao*[,1,3]

[1]Western Australia School of Mines: Minerals, Energy and Chemical Engineering (WASM-MECE), Curtin University, Perth, Western Australia 6102, Australia.

[2]School of Engineering, Edith Cowan University, 270 Joondalup Drive, Joondalup, Western Australia 6027, Australia

[3]State Key Laboratory of Materials-Oriented Chemical Engineering, College of Chemical Engineering, Nanjing Tech University, Nanjing 211816, China.

*Corresponding authors.

E-mail addresses: yijun.zhong@curtin.edu.au (Y. Zhong), zongping.shao@curtin.edu.au (Z. Shao)

Graphical abstract

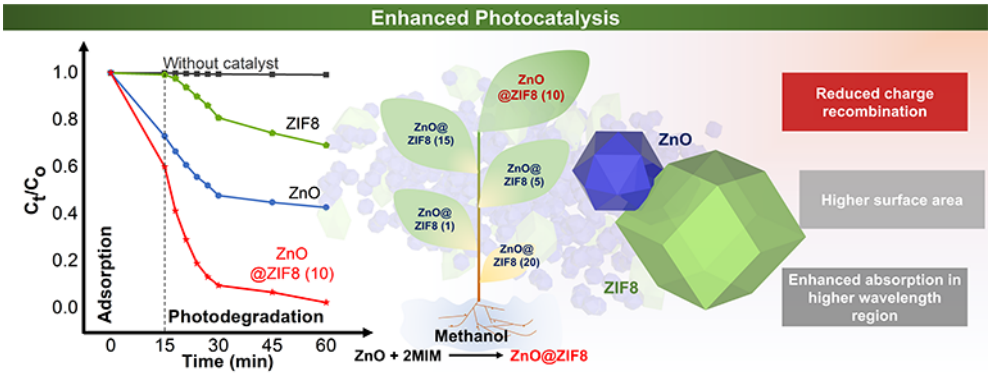

Highlights

- ZnO@ZIF8 nanoparticles (NPs) presented enhanced photocatalysis
- The composite showed retarded charge recombination and higher surface area
- Retarded charge recombination was achieved by trapping photogenerated electrons
- ZIF8 within the hybrid NPs trap these electrons
- Enhanced absorption also supplementary contribute towards improved photocatalysis

Abstract

Semiconducting zinc oxide nanoparticles (ZnO NPs) hold great potential as photocatalysts in wastewater treatment because of their favorable bandgap and cost-effectiveness. Unfortunately, ZnO NPs usually show rapid charge recombination that limits their photocatalytic efficacy significantly. Herein, we report a facile way of modifying ZnO NPs with zeolite imidazole framework-8 (ZIF8). A synergy between the two components may tackle the drawback of fast charge recombination for pristine ZnO NPs. Improved performance of photocatalytic degradation of methylene blue (MB) is confirmed by comparing with pristine ZnO and ZIF8 as the catalysts. The ZIF8 in the composite serves as a trap for photogenerated electrons, thus reducing the rate of charge recombination to enhance the photocatalysis rate. In addition, the hybridization process suppresses the aggregation of ZnO NPs, providing a large surface area and a greater number of active sites. Moreover, a small shift in the absorption band of ZnO@ZIF8 (10) NPs towards higher wavelength, also witnessed a little contribution towards enhanced photocatalytic properties. Mechanistic studies of the photocatalytic process of MB using ZnO@ZIF8 NPs catalyst reveal that hydroxyl radicals are the major reactive oxygen species. The facile hybridization of ZnO with ZIF8 provides a strategy for developing new photocatalysts with wide application potential.

Keywords: semiconductor-zeolite imidazole nanoparticle; photocatalyst; photocatalysis; charge recombination; wastewater treatment

1. Introduction

Energy and environmental technologies are important for sustainable development [1-4]. Toxic industrial wastes create contemporary environmental problems owing to the property of their carcinogenic, persistent, and bio-accumulative [5-8]. Due to the rising worry over water pollution, there is an urgent need to create efficient solutions to remove environmental concerns. Semiconductor photocatalysis is an imperative technique for the abatement of organic pollutants in wastewater [9-12]. Owing to many favourable physical and chemical characteristics, including wide bandgap (3.34 eV), high excitation binding energy (60 meV), high mobility of electrons, chemical and thermal stability, non-toxicity, recyclability, cost-effectiveness, and environmental friendliness. ZnO NPs have been widely employed as catalysts in photocatalysis, in particular for the degradation of organic pollutants [13-16]. However, one of the major drawbacks is the fast recombination of photoinduced electron-hole pairs, which results in reduced quantum efficiency of photocatalyst due to waste of energy in the form of light or heat [17, 18]. To achieve the widespread utilization of ZnO NPs in

photocatalysis, researchers have developed several strategies to improve their performance [19-22]. For example, trapping the photogenerated electrons or holes has been widely applied to hinder the recombination of charge carriers, thereby increasing their lifespan and allowing redox processes to proceed more easily [23].

There are many ways to realize charge carrier trapping, such as metal (oxide) doping [24, 25], and hybrid composites with other materials [26]. Saleh et al. [24] tried manganese/cobalt doping into ZnO NPs via a co-precipitation method, and the doping resulted in a charge trapping effect with retarded charge recombination and enhanced photocatalytic properties. Ba-Abbad et al. [27] also found significant improvement in photocatalysis with a small amount of iron doping into a ZnO matrix. In another study, Divband et al. [28] developed Ag/ZnO photocatalysts by polyacrylamide gel method and studied the mechanism of electron trapping with the introduction of Ag for improved photocatalysis. In addition to doping strategy, the formation of composite could also increase the charge separation (i.e., reduced charge recombination). For example, due to their difference in electrical potential, e.g., the higher conduction band (CB) of ZnO as compared with carbon material, the formation of carbon-based hybrid nanomaterials with ZnO demonstrated improving photocatalysis [29]. The carbon materials acted as a reservoir to entrap photogenerated electrons to hinder charge recombination [26]. Carbon nanomaterials also played an important role in both electron-accepting and electron-transporting media, thus significantly aiding in the quick transport of photo-induced charge carriers, thereby enhancing photocatalysis [30]. However, conventional synthetic procedures typically involve complex procedures, critical conditions, and high costs. A facile, large scalable, and economic synthesis method is still urgently needed.

Metal-organic framework based composites (e.g., ZIF8-based composites) are an emerging class of porous materials that have been extensively investigated for applications in different fields, including adsorption, electrocatalysis, and heterogeneous catalysis, because of their merits including large specific surface area (~2000 m^2 g^{-1}), high porosity, and defined and tuneable composition [31-35]. The regular porous structure of ZIF8 provides the opportunity to form a stable matrix with massive active sites, and may potentially enhance photocatalytic performance due to the caging effect [36] and enlarged surface area [37]. It also provides a thermally stable material [38].

In this study, we reported a rational design of ZnO@ZIF8 NPs nanocomposite as a promising photocatalyst for efficient breaking down of organic contaminants. A facile wet-

chemical way was provided for forming ZnO@ZIF8 hybrid materials. The hybridization resulted in reduced charge recombination that is credited to the electron trapping potential of ZIF8. Moreover, the porous ZIF8 provides a large surface area thus providing a higher number of an active and ultimate larger production of ROS. On the other hand, a shift in absorption potential towards higher wavelength also suggests larger production of charge carriers. As a result of these three advantageous properties, better photocatalysis for dye degradation was achieved by the composite catalyst compared to the individual components. The reaction mechanism was also further studied. ZnO and ZIF8 nanocomposite may provide useful inspiration for the development of efficient photocatalysts with wide application potential.

2. Experimental

2.1 Materials synthesis and characterization

All the chemicals in this study were purchased from Sigma-Aldrich, Australia, and used as received without further purification. Deionized (DI) water was applied in all experiments. For the preparation of the ZnO@ZIF8 PSs, 0.5 mmol of zinc nitrate hexahydrate, 3 mmol of 2-MIM, and 0.3 mmol ZnO NPs were mixed in 30 mL methanol. The resulting solution was mechanically stirred and heated at 70 °C for 20 min until the reactants were evenly dispersed. The mixture was cooled naturally to room temperature. ZnO@ZIF8 NPs were harvested by centrifugation and then dried at 80 °C overnight. Five different composites ZnO@ZIF8 (1), ZnO@ZIF8 (5), ZnO@ZIF8 (10), ZnO@ZIF8 (15), ZnO@ZIF8 (20) were prepared by increasing the loading of ZnO NPs by a factor of 5, 10, 15, and 20 (i.e., 0.3 mmol, 1.5 mmol, 3.0 mmol, 4.5 mmol, and 6 mmol ZnO NPs), respectively. For comparison, ZIF8 NPs were synthesized using similar schematics of ZnO@ZIF8 NPs.

To identify the crystal structures of the various as-prepared ZnO@ZIF8 NPs, a Bruker D8A–advance apparatus was used with integrated Cu Kα radiation at the conditions of λ value of 1.54178 Å, the potential of 40 kV, and current of 40 mA to conduct X-ray diffraction (XRD) studies over a 2θ range of 10-80 °. To examine the sample particulate morphology, electron scanning microscopy (SEM, Zeiss Clara) was used. Selected samples were also examined by a transmission electron microscope (TEM) equipped with dispersive X-ray spectroscopy (EDX) (JEOL JSM 2011).

To get information about total organic carbon, a Rock-Eval 6 total organic carbon (TOC) analyzer was utilized to quantify the organic linker of pure and composite ZIF8 samples.

Thermal gravimetric analysis (TGA) was performed to check the thermal stability of synthesized materials using PerkinElmer Pyris 1 TGA. The samples were heated to 700 °C under airflow (20 mL min^{-1}) conditions. The specific surface areas of the samples were measured using Micromeritics Tristar II plus based on the nitrogen (N_2) adsorption-desorption isotherms and calculated based on the Brunauer–Emmett–Teller (BET) method. The UV-Vis diffuse reflectance spectra (DRS) of NPs were obtained using $BaSO_4$ as a reference on the Jasco V670 spectrophotometer. A wavelength range from 350-500 nm was measured using a 2 nm bandwidth. PerkinElmer LS55 was used to collect PL spectra. The in-situ recording of photoreactive radicals was carried out using electron paramagnetic resonance (EPR) spectroscopy (Bruker EMS-plus).

2.2 Photocatalytic performance evaluation

The photocatalytic properties of developed ZnO@ZIF8 NPs were evaluated by calculating the degradation efficiency of MB. For comparison, the potential of ZIF8 and ZnO NPs in dye degradation was also investigated. All the dye degradation testings were performed in a double jacketed batch reactor at 25 °C. The introduction of a fixed amount of MB aqueous solution (10 ppm, 200 mL) and NPs suspension (45 mg L^{-1}) initiated an adsorption reaction in dark under magnetic stirring to guarantee homogeneous solution throughout the reaction. The adsorption reaction was continued for 15 min that was followed by photoirradiation for 45 min using an MSR 575/2 metal halide lamp (575 W, Philips, 315-1050 nm). Periodically, an equal amount of the sample aliquots was withdrawn by syringe and passed through a 0.45 μm Millipore syringe filter, and then the filtrate was analyzed through UV-Vis spectrometry (PerkinElmer, Lambda 25). The time-dependent absorption at 664 nm was recorded. The adsorption percentage was calculated using the following formula:

$$\%\, Removal = \frac{C_0 - C_t}{C_0} \times 100\%$$

where, C_t is the concentration of MB at a certain time, C_o is the concentration of MB at time zero. The photodegradation was calculated by recording the ratio of the MB concentration at a certain time and MB concentration at t=15 min (C_o').

3. Results and discussion

3.1 Morphological structure

A typical procedure for the preparation of ZnO@ZIF8 is schematically shown in **Fig. 1**. During the synthesis process, ZnO NPs served as self-templates to provide supplementary Zn^{2+} in a methanol solution containing 2-MIM and zinc nitrate [39]. The coordination of Zn^{2+} with 2-MIM resulted in the formation of ZIF8 by nucleation and growing process. The successful preparation of ZnO@ZIF8 composites was first supported by XRD characterization. The corresponding patterns of the various ZnO@ZIF8 NPs nanocomposites are shown in **Fig. 2a**, which confirm the presence of both ZnO (ICDD ID: 00-036-1451) [40] and ZIF8 (ICDD ID: 00-062-1030) [41]. Relatively strong diffraction peaks appearing here suggest the high crystallinity of ZnO@ZIF8 NPs. It is noted that some small peaks with low in density in the XRD patterns of ZnO@ZIF8 (15) were difficult to index. Furthermore, the FTIR spectra also demonstrated the evolution of the composite structure. In the ZnO@ZIF8 NPs (**Fig. 2b**), the Zn-O moiety's stretching band at 420 cm^{-1} [38] was observed, whereas the planes bending and stretching bands for the imidazole at 500-1350 cm^{-1} and 1350-1500 cm^{-1}, respectively [42], were also detected. In addition, the stretching vibrational band of C–N at around 1584 cm^{-1} [43], was also appeared.

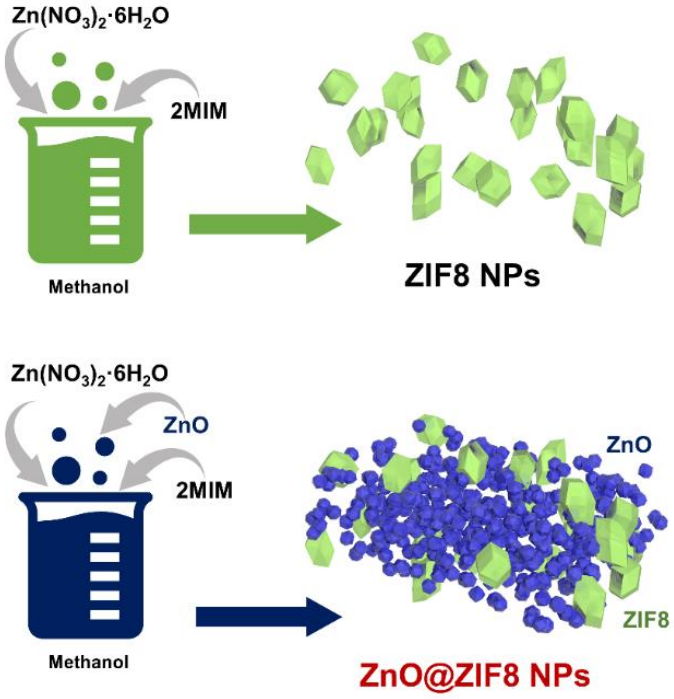

Fig. 1: Schematics of the synthesis procedures of ZIF8 NPs and ZnO@ZIF8 NPs.

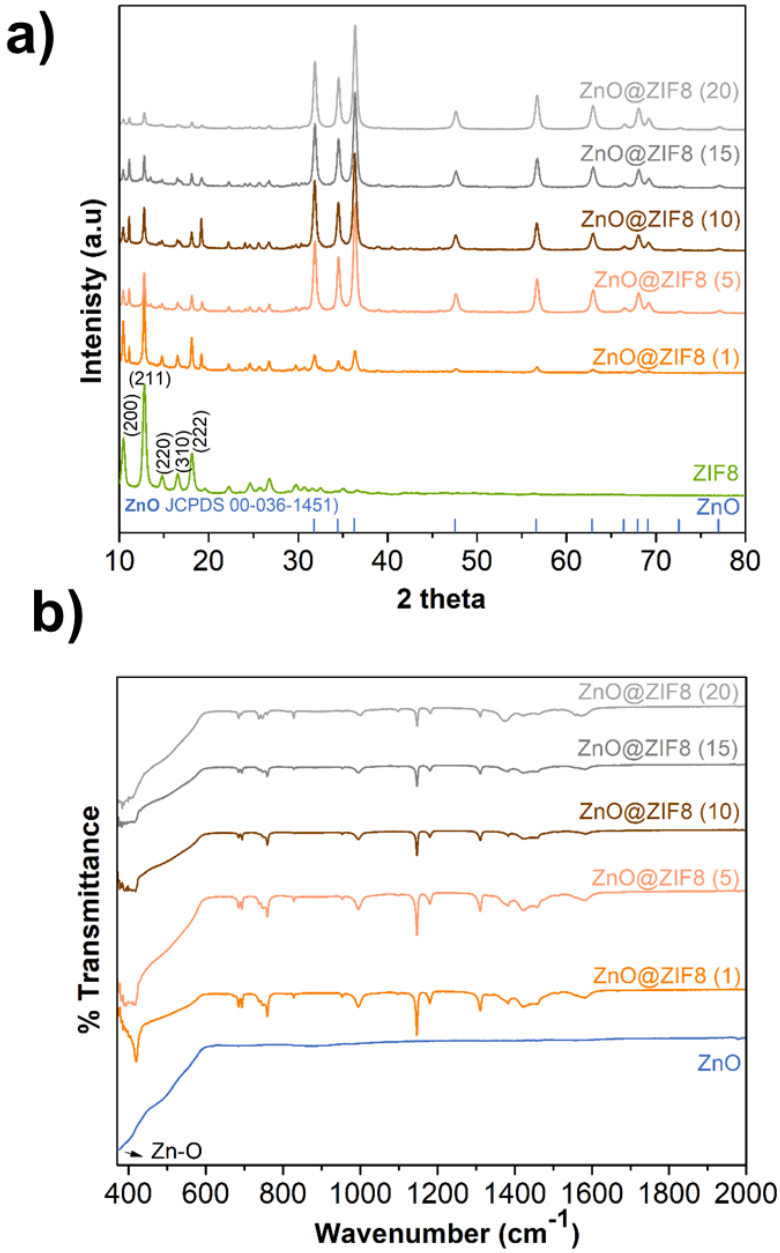

Fig. 2: a) XRD, b) FTIR images of ZnO@ZIF8 NPs.

The morphologies of the nanocomposites with different ZnO:ZIF8 ratios were observed by TEM (**Fig. 3a-e**). The samples present similar morphology with a particle size of 25-50 nm. The increased amount of ZnO added to the synthesis mixtures resulted in a higher ratio of ZnO:ZIF8 in the ZnO@ZIF8 composite. TOC analysis (**Fig. 3f**) provides supportive evidence where it shows a decrease in organic contents with an increase of ZnO loadings. The weight ratio of ZnO and ZIF8 in the ZnO@ZIF8 (10) composite was further evaluated by TGA under an airflow condition (**Fig. 3f inset**)**.** The TGA profile of ZnO confirmed it was thermally stable without a significant weight loss at 700 °C. The previous publication indicated that the

oxidation of ZIF8 at high temperature may form gaseous products (e.g., CO_2, NO_x, H_2O) and zinc oxide [41]. Based on these thermal behaviors of ZnO and ZIF8 and the residual weight of 87.9% for the ZnO@ZIF8 (10) composite, the weight percentage of the ZnO and the ZIF8 in the ZnO@ZIF8 (10) composite were calculated to be 81.2% and 18.8%.

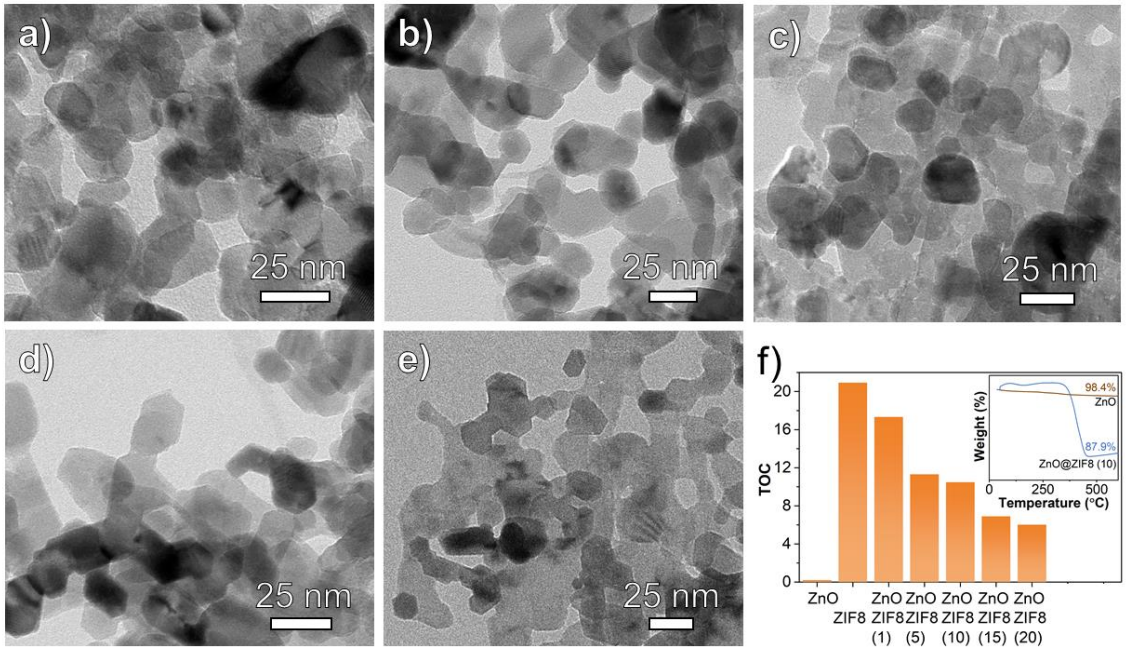

Fig. 3: TEM images of a) ZnO@ZIF8 (1), b) ZnO@ZIF8 (5), c) ZnO@ZIF8 (10), d) ZnO@ZIF8 (15), and e) ZnO@ZIF8 (20) NPs, and f) TOC of ZnO@ZIF8, ZIF8, and ZnO NPs, inset: TGA of ZnO and ZnO@ZIF8 (10) NPs.

To further confirm the morphology and hybrid nature, ZnO@ZIF8 (10) NPs were selected as the representative sample and further characterized by high-resolution electron microscopy (HRTEM). As shown in **Fig. 4a**, the sample is in the crystalline phase, and lattice spacing of 0.45 and 0.53 nm were observed from different positions of the sample, which match that of the (321) plane of ZnO NPs, and (310) plane of ZIF8, respectively. This result demonstrated the distribution of ZnO and ZIF8 in the nanocomposite. Moreover, the selected area electron diffraction (SAED) images (**Fig. 4b**) revealed circular diffraction patterns referred to (100), (110), and (103) planes of wurtzite structure of ZnO, and (884), (631), (321), (431), (440), and (622) planes of the cubic phase of ZIF8. The chemical composition and element distribution of the ZnO@ZIF8 NPs (10) were further illustrated by the elemental mapping analysis using a high-angle annular dark-field scanning TEM (HAADF-STEM). **Fig .4c-d** reinforces the existence of both ZnO NPs and ZIF8 NPs in the composite. Note that N and C are two main elements in 2-MIM which only exist in the ZIF8 crystals. The N (blue), C (red) signals in the elemental mappings (**Fig. 4d**) indicate ZIF8 NPs were dispersed on ZnO NPs. All above results

present solid evidence to validate the successful development of the hybrid ZnO@ZIF8 NPs nanocomposite.

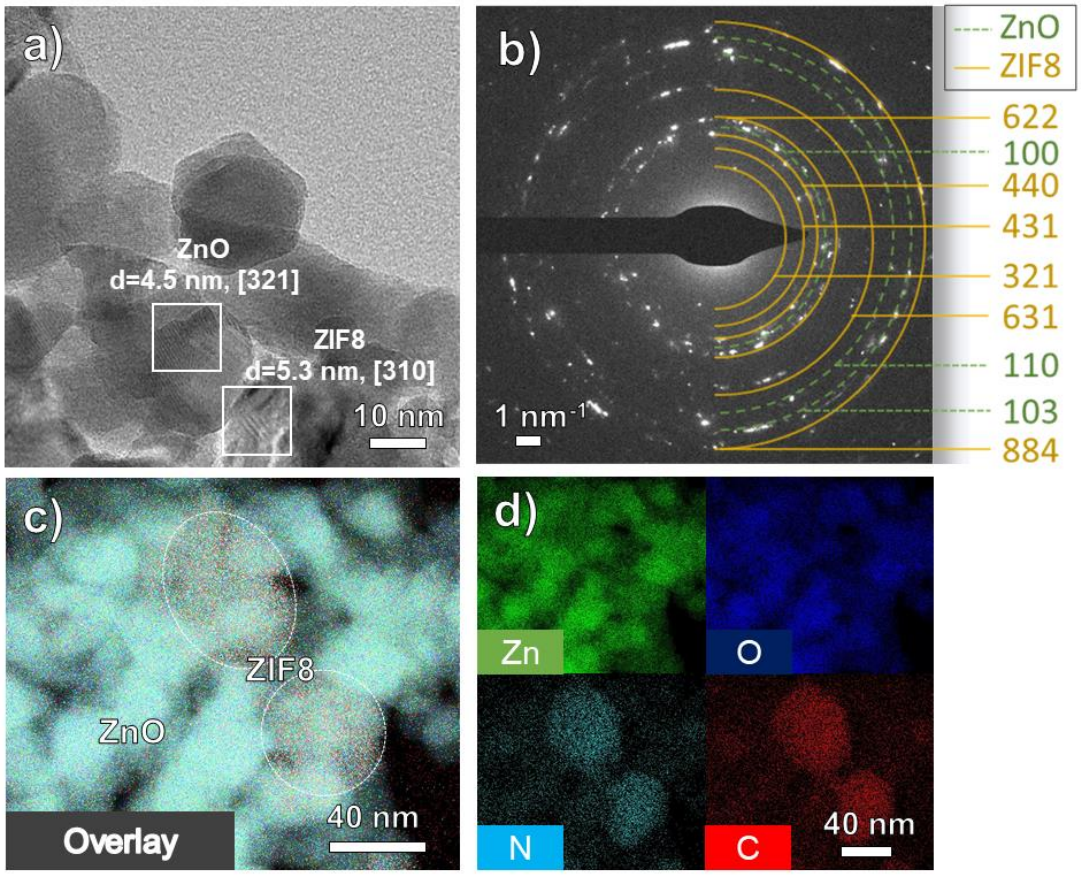

Fig. 4: a) HRTEM and corresponding b) SAED and c,d) HAADF-STEM image and corresponding elemental mapping analysis of ZnO@ZIF8 (10).

3.2 Photocatalytic performance

The photocatalytic performance of the as-synthesized ZnO@ZIF8 NPs was then assessed in terms of MB degradation, and comparative studies were also executed on ZIF8 and ZnO NPs. First, the adsorption capability of the catalysts for the dye was examined. The NPs were stirred in dark for 15 min to achieve saturated adsorption-desorption of the positively charged dye molecules [44] on the surface of the negatively charged NP, and the adsorption percentages of NPs were shown in **Fig. 5a, left**. The percentages of MB as adsorbed ZnO@ZIF8 (1), ZnO@ZIF8 (5), ZnO@ZIF8 (10), ZnO@ZIF8 (15) and ZnO@ZIF8 (20) NPs were 38.46%, 37.74 %, 39.90%, 34.13 %, and 38.96 %, respectively. It suggests no big difference in the adsorption capability of the various ZnO@ZIF8 nanocomposites with different ZnO to ZIF8 ratios, which is attributed to the negligible difference in their zeta-potential. The obtained zeta-potential values of ZnO@ZIF8 (1), ZnO@ZIF8 (5), ZnO@ZIF8 (10), ZnO@ZIF8 (15) and

ZnO@ZIF8 (20) NPs were -19.53, -19.9, -22.16, -17.1, -16.8, respectively (**Fig. 5b**). Thus, the difference in the later photocatalytic activity could be mainly ascribed to the difference in their intrinsic activity. Interestingly, ZIF8 (zeta-potential: -2.5) alone showed almost negligible dye adsorption, while pristine ZnO (zeta-potential: -4.33) showed lower dye adsorption than the various nanocomposites. It suggests dye was mainly adsorbed over the ZnO surface, while the hydrazination between ZnO and ZIF8 led to increased dye adsorption. It suggests the hydrazination process likely suppressed the aggregation of ZnO NPs, thus increasing the surface area (ZnO: 33 m^2/g, ZnO@ZIF8: 200-350 m^2/g) for dye adsorption.

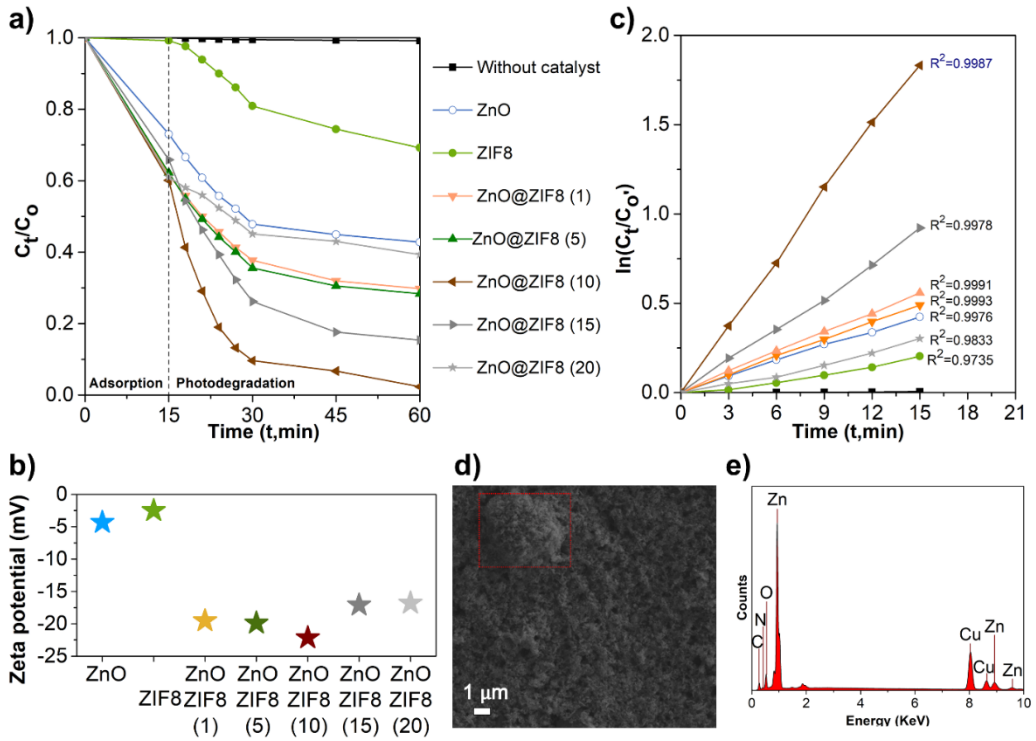

Fig. 5: a) Adsorption of MB over 15 min in dark (left) and photocatalysis over 45 min under light (right), b) zeta-potentials of ZnO@ZIF8, ZIF8, and ZnO NPs, c) pseudo-first-order linear plots of the photocatalysis kinetics of MB using ZnO@ZIF8, ZIF8, and ZnO NPs, d) SEM image and e) corresponding EDS spectrum of a selected region of ZnO@ZIF8 (20) NPs.

Photocatalytic degradation of MB over the various catalysts was conducted for a fixed period of 45 min under the same photo illumination of 315–1050 nm. The as-synthesized ZnO NPs showed much lower photocatalytic efficiency of only 57.21 %, as compared with ZnO@ZIF8 (1), ZnO@ZIF8 (5), ZnO@ZIF8 (10), ZnO@ZIF8 (15) and ZnO@ZIF8 (20) NPs (70.18%, 71.62 %, 97.65%, 84.60 %, and 60.67 %, respectively) (**Fig. 5a, right**). Furthermore, upon analysis, the photocatalytic degradation of MB followed pseudo-first-order kinetics,

studied by plotting $\ln(C_o'/C_t) = kt$ as shown in **Fig. 5c**, where the rate constant k (min^{-1}) is equal to the slope of the fitting line, C_0' and C_t correspond to the equilibrium and time t concentration of MB molecules, respectively. With the increase in ZnO NPs loading, the photocatalysis rate increased in the sequence of ZnO@ZIF8 (1), ZnO@ZIF8 (5), and ZnO@ZIF8 (10) NPs (**Fig. 5a, right**). This improvement may benefit from the strategy adopted in the synthesis, where the ZnO NP served as a supplemental Zn^{2+} source for the growth of ZIF8 on the ZnO. As a result, a good attachment between ZnO NPs and ZIF8 NPs can be achieved. It is worth noting that the growth of ZIF8 is highly dependent on the Zn^{2+} release rate from the ZnO and the coordination rate of Zn^{2+} with 2-MIM [45]. Therefore, the initial loading amount of ZnO NPs is vital for the tuning of compositional ratio and integration of ZnO and ZIF8 in the resulting ZnO/ZIF8 composites. The optimized composite for best photocatalytic performance was achieved when the loading of ZnO is of factor 10 (2-MIMs/Zn^{2+} ratio=0.86) for ZnO@ZIF8 (10). In the synthesis process, the Zn^{2+} release and the coordination of Zn^{2+} and 2MIM are competitive processes [46]. When the ZnO loading was further increased, the releasing rate of Zn^{2+} also further increased while the coordination rate was not sufficient, which could result in a large quantity of unreacted agglomerated ZnO NPs (**Fig. 5d**) [47, 48]. As a result, ZnO@ZIF8 (15) and ZnO@ZIF8 (20) presented inferior performance compared to ZnO@ZIF8 (10). The EDS mapping (**Fig. 5e**) on a selected region ZnO@ZIF8 (20) NPs also countersigned that the agglomerated particles are ZnO.

The outstanding photocatalytic performance of ZnO@ZIF8 (10) NPs can be explained by the following three main reasons: (1) reduced charge recombination, (2) large surface area, and (3) high absorption values. Firstly, the reduced charge recombination could be attributed to the higher LUMO (lowest unoccupied molecular orbital) level of ZIF8 as compared with CB of ZnO hinder electron transport thus, hindering the charge recombination [49]. Also, the N-Me-O bond formed at the interface of Me and ZIF8 tends to greatly reduce the photo-induced electron-hole pairs recombination [50]. Moreover, the reduced charge recombination might also be associated with the oxygen vacancy in the composite [51] which reduces the charge recombination centers [52]. For confirming the above aspects, PL spectra of ZnO and ZnO@ZIF8 (10) were analyzed. Compared with pure ZnO NPs, a hypochromic shift in the PL peak of ZnO@ZIF8 (10) can be observed (**Fig. 6a**). This indicates a slow recombination rate which results in higher electron-hole separation [53]. It is also worth mentioning that the PL spectra are also very sensitive to the crystal structures and the surface defects [54], such as

oxygen vacancy [55]. The low recombination rate of photoinduced charge carriers could be the key aspect for improving the photocatalytic performance [56].

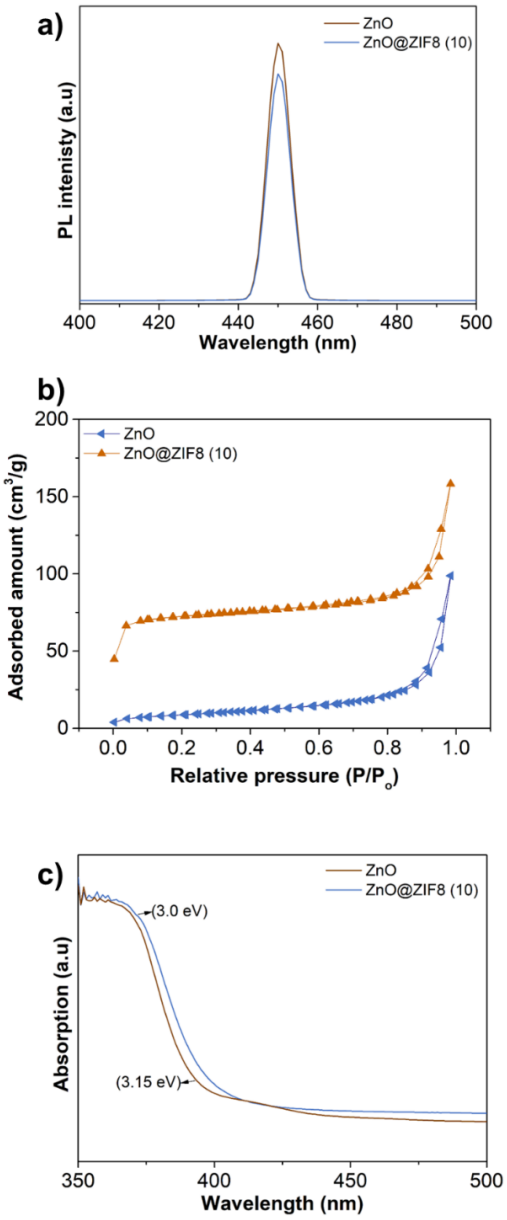

Fig. 6: a) PL spectra of ZnO and ZnO@ZIF8 (10) NPs at excitation wavelength 450 nm, b) nitrogen adsorption-desorption isotherms and c) DRS spectra of ZnO and ZnO@ZIF8 (10) NPs.

A higher specific BET surface area (256 $m^2 g^{-1}$) [57, 58] was observed for the ZnO@ZIF8 (10) sample (**Fig. 6b**) was the second reason for the outstanding photocatalytic performance. The high surface area provides more active sites to generate much enhanced photo-excited charge carriers and the ultimately large quantity of ROS production [59-61]. The formation of ZnO@ZIF8 nanocomposites effectively suppressed the aggregation of ZnO nanoparticles.

The shifting in absorption potential towards higher wavelength values could be the third reason for enhanced photocatalytic performance. **Fig. 6c** showed a small shifting of the DRS peak towards a higher wavelength for ZnO@ZIF8 when compared with ZnO NPs. It suggests the large production of charge carriers [62], which also presented a certain contribution towards enhanced photocatalysis.

A comparison of the current activity with some representative literature results is provided in **Table 1**. The ZnO@ZIF8 (10) sample in this work presented an outstanding photocatalytic performance among other ZnO-based photocatalysts, further confirming the effectiveness of our material in water treatment.

Table 1: Comparison of catalytic performances of ZnO@ZIF8 NPs and some other photocatalysts for the photocatalysis process.

No	Material	Catalyst loading	Dye	Dye concentration	Time	Degradation	Ref
		mg/L		Ppm	Min	%	
1	ZnO@ZIF8	45	MB	10	45	98	This work
2	La@ZnO	100	Rh B	N/A	78	99	[63]
3	ZIF derived ZnO	25	MB	10	120	99	[64]
4	ZIF-8 covered Zn-Al	400	MB	10	180	80	[65]
5	MOF@rGO	25	MB	N/A	120	70	[66]

Note: Rh: Rhodamine dye

To scrutinize the mechanism of photocatalytic degradation, EPR spectra were performed *using* 5-dimethyl-1-pyrroline-N-oxide (DMPO), and 2,2,6,6-tetramethylpiperidine (TEMP) as a probe of singlet oxygen ($^1O_2$) and hydroxyl radicals (•OH) [67, 68]. Four characteristic peaks were observed in •OH-DMPO EPR spectra (**Fig. 8a**) [69] while three characteristic peaks were detected for $^1O_2$-TEMP (**Fig. 8b**) [70], verifying that •OH and $^1O_2$ acted as the main reactive oxygen species (ROS) during the degradation of MB. This can be further verified by an active species trapping experiment, using tert-butyl alcohol (tBA), sodium azide (NaN_3), and benzoquinone (BQ) as a scavenger of •OH, $^1O_2$, and superoxide radicals ($\bullet O_2^-$), respectively [71, 72]. **Fig. 8c** showed a sharp decline with the addition of tBA and NaN_3 while the presence of BQ had no significant change on the photocatalytic performance as compared with that of ZnO@ZIF8 (10) without a scavenger. The scavengers were quenched in the respective order: BQ (43%) > NaN_3 (81%) > tBA (97%) at t=45 min. Thus, it can be seen that •OH play the key roles in the degradation of MB as compared with $^1O_2$ and $\bullet O_2^-$.

The photocatalytic degradation phenomenon of ZnO@ZIF8 is schematically shown in **Fig. 8d**. Electrons were generated at the CB and holes were generated at the valence band (VB) of both ZnO and ZIF8. After that, the electrons may transfer from the excited state to the ZnO

then react with oxygen molecules, and the holes react with •OH on the surface of the ZIF8 [73, 74].

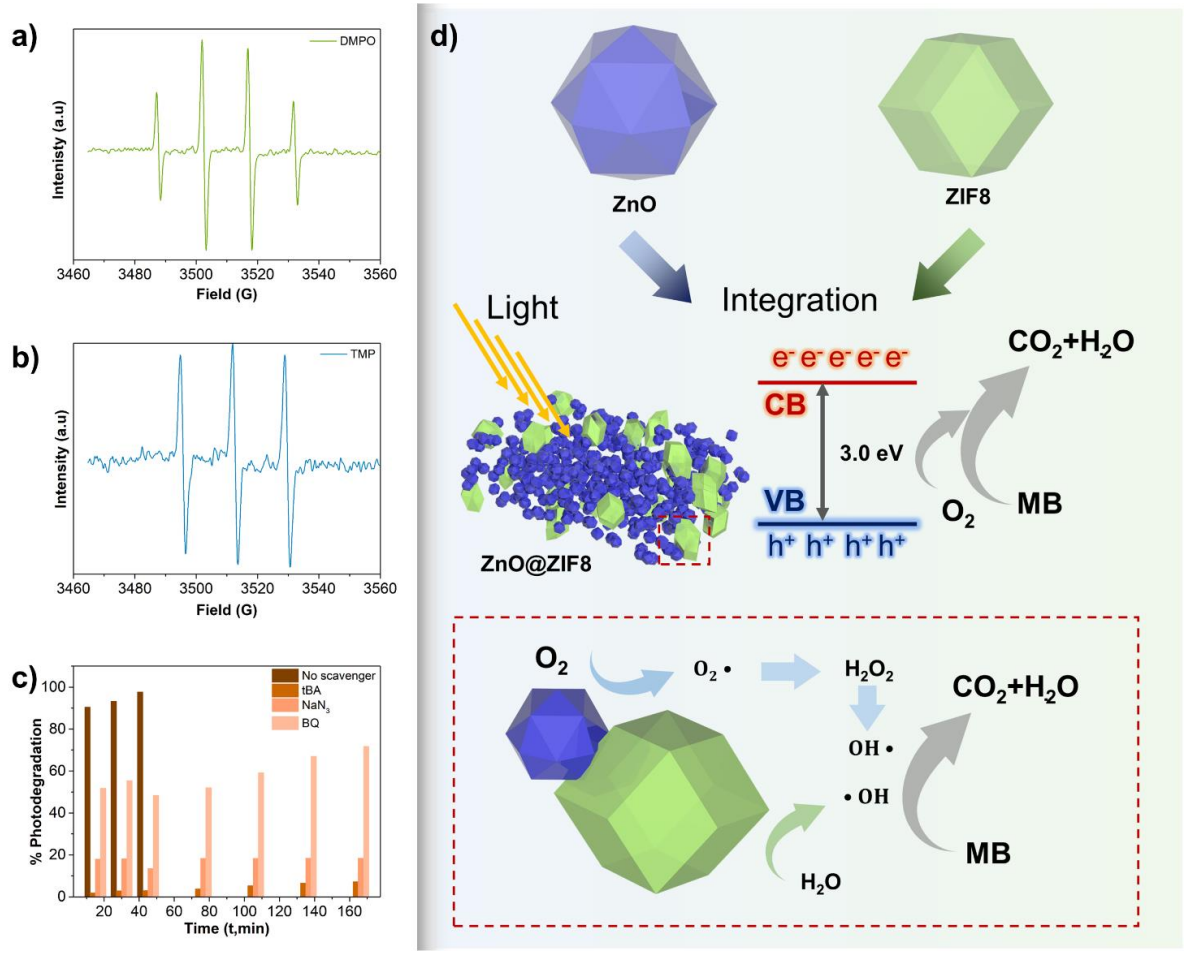

Fig. 7: EPR testing using a) DMPO, b) TMP, c) scavenger test using ZnO@ZIF8 (10) NPs with tBA, NAN_3, and BQ, and d) mechanism of MB degradation by ZnO@ZIF8 NPs.

4. Conclusion

In conclusion, we have prepared ZnO@ZIF8 hybrid NPs via a facile synthesis process. As a photocatalyst in the dye degradation experiment, ZnO@ZIF8 NPs presented outstanding performance with the dye degradation efficiency of 98% within 45 minutes, much superior to that with the pure ZnO NPs (efficiency of 57%). The enhanced photocatalysis was attributed to the reduced charge recombination rate, which was ascribed to the photogenerated electrons tapping the potential of ZIF8. Also, the significantly larger specific surface area (256 m^2 g^{-1}) of ZnO@ZIF8 NPs than that of ZnO NPs (31 m^2 g^{-1}) suggests the effectively suppressed aggregation of the ZnO phase from the hydrazination, thereby improving the quantum efficiency of the photocatalytic process from increase active sites. Moreover, a shift in

absorption potential of ZnO@ZIF8 (10) NPs can lead to the lower gap which contributes to the enhanced photocatalytic properties. The EPR and quenching tests proved that •OH is the main ROS for MB degradation over ZnO@ZIF8 NPs. The findings obtained in this study provide new thinking for the development of efficient photocatalysts for various applications.

Acknowledgments

This work was supported by the Australian Research Council Discovery Project, Grant No. DP200103332 and DP200103315.

Declaration of competing interest

The authors declare that they have no known competing financial interests or personal relationships that could have appeared to influence the work reported in this paper.

References

[1] H. Fatima, Y. Zhong, H. Wu, Z. Shao, Recent advances in functional oxides for high energy density sodium-ion batteries, Materials Reports: Energy 1(2) (2021) 100022.
[2] F. Lira, I. Vaz-Moreira, J. Tamames, C.M. Manaia, J.L. Martínez, Metagenomic analysis of an urban resistome before and after wastewater treatment, Scientific Reports 10 (2020) 8174.
[3] L. Wu, D. Ning, B. Zhang, Y. Li, P. Zhang, X. Shan, Q. Zhang, M.R. Brown, Z. Li, J.D. Van Nostrand, Global diversity and biogeography of bacterial communities in wastewater treatment plants, Nature Microbiology 4(7) (2019) 1183-1195.
[4] P. Vairale, V. Sharma, B. Bade, A. Waghmare, P. Shinde, A. Punde, V. Doiphode, R. Aher, S. P, h. harkar, S. Nair, V. Jadkar, Melanin Sensitized Nanostructured ZnO Photoanodes for Efficient Photoelectrochemical Splitting of Water: Synthesis and Characterization, Engineered Science 11 (2020) 76-84.
[5] A. Sheikhmohammadi, E. Asgari, M. Manshouri, The synergistic effect of O_3 and H_2O_2 on the Butyl p-hydroxybenzoate photo-catalytic degradability by UVC/ZnO: Efficiency, kinetic, pathway, mechanism, Optik 239 (2021) 166673.
[6] N. Liu, Y. Zheng, C. Jing, B. Gao, W. Huang, Z. Li, J. Lei, X. Zhang, L. Cui, L. Tang, Boosting catalytic degradation efficiency by incorporation of MIL-53 (Fe) with $Ti_3C_2T_x$ nanosheeets, Journal of Molecular Liquids 311 (2020) 113201.
[7] A. Ikhlaq, M. Kazmi, A. Tufail, H. Fatima, K.S. Joya, Application of peanut shell ash as a low-cost support for Fenton-like catalytic removal of methylene blue in wastewater, Desalination and Water Treatment 111 (2018) 338-344.
[8] Y.M. Hunge, A.A. Yadav, S.-W. Kang, H. Kim, Photocatalytic degradation of tetracycline antibiotics using hydrothermally synthesized two-dimensional molybdenum disulfide/titanium dioxide composites, Journal of Colloid and Interface Science 606 (2022) 454-463.
[9] O.A. Arotiba, B.O. Orimolade, B.A. Koiki, Visible light–driven photoelectrocatalytic semiconductor heterojunction anodes for water treatment applications, Current Opinion in Electrochemistry 22 (2020) 25-34.

[10] F. Almeida, E.C. Grzebielucka, S.R.M. Antunes, C.P.F. Borges, A.V.C. Andrade, É.C.F. Souza, Visible light activated magnetic photocatalysts for water treatment, Journal of Environmental Management 273 (2020) 111143.
[11] Y.M. Hunge, A.A. Yadav, S. Khan, K. Takagi, N. Suzuki, K. Teshima, C. Terashima, A. Fujishima, Photocatalytic degradation of bisphenol A using titanium dioxide@nanodiamond composites under UV light illumination, Journal of Colloid and Interface Science 582 (2021) 1058-1066.
[12] M. Yu, T. Yu, S. Chen, Z. Guo, I. Seok, A facile synthesis of Ag/TiO_2/rGO nanocomposites with enhanced visible light photocatalytic activity, ES Materials & Manufacturing 7(6) (2020) 64-69.
[13] M.E. Ashebir, G.M. Tesfamariam, G.Y. Nigussie, T.W. Gebreab, Structural, optical, and photocatalytic activities of Ag-doped and Mn-doped ZnO nanoparticles, Journal of Nanomaterials 2018 (2018) 9425938
[14] W. Zheng, R. Ding, X. Yan, G. He, PEG induced tunable morphology and band gap of ZnO, Materials Letters 201 (2017) 85-88.
[15] A.P. Shah, S. Jain, V.J. Mokale, N.G. Shimpi, High performance visible light photocatalysis of electrospun PAN/ZnO hybrid nanofibers, Journal of Industrial and Engineering Chemistry 77 (2019) 154-163.
[16] H. Fatima, M.R. Azhar, M. Khiadani, Y. Zhong, W. Wang, C. Su, Z. Shao, Prussian blue-conjugated ZnO nanoparticles for near-infrared light-responsive photocatalysis, Materials Today Energy 23 (2022) 100895.
[17] A. Bafaqeer, M. Tahir, N.A.S. Amin, Synergistic effects of 2D/2D ZnV_2O_6/RGO nanosheets heterojunction for stable and high performance photo-induced CO_2 reduction to solar fuels, Chemical Engineering Journal 334 (2018) 2142-2153.
[18] M.A. Mohamed, M. Zain, L.J. Minggu, M.B. Kassim, J. Jaafar, N.A.S. Amin, M.S. Mastuli, H. Wu, R.J. Wong, Y.H. Ng, Bio-inspired hierarchical hetero-architectures of in-situ C-doped g-C_3N_4 grafted on C, N co-doped ZnO micro-flowers with booming solar photocatalytic activity, Journal of Industrial and Engineering Chemistry 77 (2019) 393-407.
[19] J.-H. Kim, J.-H. Lee, Y. Park, J.-Y. Kim, A. Mirzaei, H.W. Kim, S.S. Kim, Toluene-and benzene-selective gas sensors based on Pt-and Pd-functionalized ZnO nanowires in self-heating mode, Sensors and Actuators B: Chemical 294 (2019) 78-88.
[20] Y. Zhang, L. Liu, B. Van der Bruggen, M.K. Leung, F. Yang, A free-standing 3D nano-composite photo-electrode—Ag/ZnO nanorods arrays on Ni foam effectively degrade berberine, Chemical Engineering Journal 373 (2019) 179-191.
[21] Y. Dai, C. Wu, Z. Wu, Z. Zhao, L. Li, Y. Lu, Z.L. Wang, Ferroelectricity-enhanced piezo-phototronic effect in 2D V-doped ZnO nanosheets, Advanced Science 6(16) (2019) 1900314.
[22] Z. Zou, X. Yang, P. Zhang, Y. Zhang, X. Yan, R. Zhou, D. Liu, L. Xu, J. Gui, Trace carbon-hybridized ZnS/ZnO hollow nanospheres with multi-enhanced visible-light photocatalytic performance, Journal of Alloys and Compounds 775 (2019) 481-489.
[23] Y. Li, C. Liao, S.C. Tjong, Recent advances in zinc oxide nanostructures with antimicrobial activities, International Journal of Molecular Sciences 21(22) (2020) 8836.
[24] R. Saleh, N.F. Djaja, Transition-metal-doped ZnO nanoparticles: Synthesis, characterization and photocatalytic activity under UV light, Spectrochimica Acta Part A: Molecular and Biomolecular Spectroscopy 130 (2014) 581-590.
[25] C. Cheng, A. Amini, C. Zhu, Z. Xu, H. Song, N. Wang, Enhanced photocatalytic performance of TiO_2-ZnO hybrid nanostructures, Scientific Reports 4 (2014) 4181.
[26] M. Maya-Treviño, J. Guzmán-Mar, L. Hinojosa-Reyes, N. Ramos-Delgado, M. Maldonado, A. Hernández-Ramírez, Activity of the ZnO–Fe_2O_3 catalyst on the degradation of Dicamba and 2, 4-D herbicides using simulated solar light, Ceramics International 40(6) (2014) 8701-8708.

[27] M.M. Ba-Abbad, A.A.H. Kadhum, A.B. Mohamad, M.S. Takriff, K. Sopian, Visible light photocatalytic activity of Fe^{3+}-doped ZnO nanoparticle prepared via sol–gel technique, Chemosphere 91(11) (2013) 1604-1611.
[28] B. Divband, M. Khatamian, G.R.K. Eslamian, M. Darbandi, Synthesis of Ag/ZnO nanostructures by different methods and investigation of their photocatalytic efficiency for 4-nitrophenol degradation, Applied Surface Science 284 (2013) 80-86.
[29] J. Mu, C. Shao, Z. Guo, Z. Zhang, M. Zhang, P. Zhang, B. Chen, Y. Liu, High photocatalytic activity of ZnO−carbon nanofiber heteroarchitectures, ACS Applied Materials & Interfaces 3(2) (2011) 590-596.
[30] C. Jia, X. Zhang, K. Matras-Postolek, B. Huang, P. Yang, Z-scheme reduced graphene oxide/TiO_2-Bronze/$W_{18}O_{49}$ ternary heterostructure towards efficient full solar-spectrum photocatalysis, Carbon 139 (2018) 415-426.
[31] M. Chin, C. Cisneros, S.M. Araiza, K.M. Vargas, K.M. Ishihara, F. Tian, Rhodamine B degradation by nanosized zeolitic imidazolate framework-8 (ZIF-8), RSC Advances 8(47) (2018) 26987-26997.
[32] H.-P. Jing, C.-C. Wang, Y.-W. Zhang, P. Wang, R. Li, Photocatalytic degradation of methylene blue in ZIF-8, RSC Advances 4(97) (2014) 54454-54462.
[33] D. Xu, Y. You, F. Zeng, Y. Wang, C. Liang, H. Feng, X. Ma, Disassembly of hydrophobic photosensitizer by biodegradable zeolitic imidazolate framework-8 for photodynamic cancer therapy, ACS Applied Materials & Interfaces 10(18) (2018) 15517-15523.
[34] W. Wang, X. Xu, W. Zhou, Z. Shao, Recent progress in metal-organic frameworks for applications in electrocatalytic and photocatalytic water splitting, Advanced Science 4(4) (2017) 1600371.
[35] W. Cheng, Y. Wang, S. Ge, X. Ding, Z. Cui, Q. Shao, One-step microwave hydrothermal preparation of Cd/Zr-bimetallic metal–organic frameworks for enhanced photochemical properties, Advanced Composites and Hybrid Materials 4(1) (2021) 150-161.
[36] D. Esken, H. Noei, Y. Wang, C. Wiktor, S. Turner, G. Van Tendeloo, R.A. Fischer, ZnO@ZIF-8: Stabilization of quantum confined ZnO nanoparticles by a zinc methylimidazolate framework and their surface structural characterization probed by CO_2 adsorption, Journal of Materials Chemistry 21(16) (2011) 5907-5915.
[37] J. He, Z. Yan, J. Wang, J. Xie, L. Jiang, Y. Shi, F. Yuan, F. Yu, Y. Sun, Significantly enhanced photocatalytic hydrogen evolution under visible light over CdS embedded on metal–organic frameworks, Chemical Communications 49(60) (2013) 6761-6763.
[38] H. Tian, H. Fan, M. Li, L. Ma, Zeolitic imidazolate framework coated ZnO nanorods as molecular sieving to improve selectivity of formaldehyde gas sensor, ACS Sensors 1(3) (2016) 243-250.
[39] J. Cravillon, R. Nayuk, S. Springer, A. Feldhoff, K. Huber, M. Wiebcke, Controlling zeolitic imidazolate framework nano-and microcrystal formation: insight into crystal growth by time-resolved in situ static light scattering, Chemistry of Materials 23(8) (2011) 2130-2141.
[40] J. Liu, M. Wang, X. Wu, Y. Chen, Dispersion of ZnO nanocrystals using ammonium polycarboxylate (AMP) for the fabrication of ZnO-based ceramics, Journal of Electronic Materials 49(5) (2020) 1-9.
[41] V.V. Butova, A.P. Budnyk, E.A. Bulanova, C. Lamberti, A.V. Soldatov, Hydrothermal synthesis of high surface area ZIF-8 with minimal use of TEA, Solid State Sciences 69 (2017) 13-21.
[42] G. Ren, Z. Li, W. Yang, M. Faheem, J. Xing, X. Zou, Q. Pan, G. Zhu, Y. Du, ZnO@ ZIF-8 core-shell microspheres for improved ethanol gas sensing, Sensors and Actuators B: Chemical 284 (2019) 421-427.

[43] X. Yang, Z. Wen, Z. Wu, X. Luo, Synthesis of ZnO/ZIF-8 hybrid photocatalysts derived from ZIF-8 with enhanced photocatalytic activity, Inorganic Chemistry Frontiers 5(3) (2018) 687-693.
[44] F. Azeez, E. Al-Hetlani, M. Arafa, Y. Abdelmonem, A.A. Nazeer, M.O. Amin, M. Madkour, The effect of surface charge on photocatalytic degradation of methylene blue dye using chargeable titania nanoparticles, Scientific Reports 8(1) (2018) 7104.
[45] X. Wang, J. Liu, S. Leong, X. Lin, J. Wei, B. Kong, Y. Xu, Z.-X. Low, J. Yao, H. Wang, Rapid construction of ZnO@ ZIF-8 heterostructures with size-selective photocatalysis properties, ACS Applied Materials & Interfaces 8(14) (2016) 9080-9087.
[46] W.-w. Zhan, Q. Kuang, J.-z. Zhou, X.-j. Kong, Z.-x. Xie, L.-s. Zheng, Semiconductor@metal–organic framework core–shell heterostructures: A case of ZnO@ZIF-8 nanorods with selective photoelectrochemical response, Journal of the American Chemical Society 135(5) (2013) 1926-1933.
[47] H. Wang, P. Zhou, R. Guo, Y. Wang, H. Zhan, Y. Yuan, Synthesis of rectorite/Fe_3O_4/ZnO composites and their application for the removal of methylene blue dye, Catalysts 8(3) (2018) 107.
[48] A. Taufik, R. Saleh, Comparison of catalytic activities for photocatalytic and sonocatalytic degradation of organic dye in the presence of ternary Fe_3O_4/ZnO/CuO magnetic heteregenous nanocatalyst, AIP Conference Proceedings 1725 (2016) 020088.
[49] H. Kim, W. Kim, J. Park, N. Lim, R. Lee, S.J. Cho, Y. Kumaresan, M.-K. Oh, G.Y. Jung, Surface conversion of ZnO nanorods to ZIF-8 to suppress surface defects for a visible-blind UV photodetector, Nanoscale 10(45) (2018) 21168-21177.
[49] A. Malik, M. Nath, S. Mohiyuddin, G. Packirisamy, Multifunctional CdSNPs@ ZIF-8: Potential antibacterial agent against GFP-expressing Escherichia coli and Staphylococcus aureus and efficient photocatalyst for degradation of methylene blue, ACS Omega 3(7) (2018) 8288-8308.
[50] X. Zeng, L. Huang, C. Wang, J. Wang, J. Li, X. Luo, Sonocrystallization of ZIF-8 on electrostatic spinning TiO_2 nanofibers surface with enhanced photocatalysis property through synergistic effect, ACS Applied Materials & Interfaces 8(31) (2016) 20274-20282.
[51] Y. Li, S. Xiao, W. Li, X. He, W. Fang, H. Chen, J. Ge, L. Zhao, ZnO@ZIF-8 inverse opal structure photoanode for efficient CdS/CdSe co-sensitized quantum dot solar cells, Journal of Materials Science 55(17) (2020) 7453-7463.
[52] C. Wang, D. Wu, P. Wang, Y. Ao, J. Hou, J. Qian, Effect of oxygen vacancy on enhanced photocatalytic activity of reduced ZnO nanorod arrays, Applied Surface Science 325 (2015) 112-116.
[53] A. Malik, M. Nath, S. Mohiyuddin, G. Packirisamy, Multifunctional CdSNPs@ZIF-8: potential antibacterial agent against GFP-expressing Escherichia coli and Staphylococcus aureus and efficient photocatalyst for degradation of methylene blue, ACS Omega 3(7) (2018) 8288-8308.
[54] G.-Q. Tang, Y. Xiong, L.Z. Zhang, G.-L. Zhang, Novel long-lifetime photoluminescence of nanosized ZnO included in the mesoporous MCM-41, Chemical Physics Letters 395(1-3) (2004) 97-102.
[55] B. Choudhury, A. Choudhury, Oxygen vacancy and dopant concentration dependent magnetic properties of Mn doped TiO_2 nanoparticle, Current Applied Physics 13(6) (2013) 1025-1031.
[56] C. Ma, J. Lee, Y. Kim, W. Cheol Seo, H. Jung, W. Yang, Rational design of α-Fe_2O_3 nanocubes supported $BiVO_4$ Z-scheme photocatalyst for photocatalytic degradation of antibiotic under visible light, Journal of Colloid and Interface Science 581 (2021) 514-522.

[57] Y. Zhong, X. Xu, J.-P. Veder, Z. Shao, Self-recovery chemistry and cobalt-catalyzed electrochemical deposition of cathode for boosting performance of aqueous zinc-ion batteries, iScience 23(3) (2020) 100943.
[58] J. Singh, A. Kalamdhad, Effects of heavy metals on soil, plants, human health and aquatic life, International Journal of Research in Chemistry and Environment 1(2) (2011) 15-21.
[59] F. Wang, Y. Zhou, X. Pan, B. Lu, J. Huang, Z. Ye, Enhanced photocatalytic properties of ZnO nanorods by electrostatic self-assembly with reduced graphene oxide, Physical Chemistry Chemical Physics 20(10) (2018) 6959-6969.
[60] A. Mclaren, T. Valdes-Solis, G. Li, S.C. Tsang, Shape and size effects of ZnO nanocrystals on photocatalytic activity, Journal of the American Chemical Society 131(35) (2009) 12540-12541.
[61] J. Bogdan, J. Pławińska-Czarnak, J. Zarzyńska, Nanoparticles of titanium and zinc oxides as novel agents in tumor treatment: a review, Nanoscale Research Letters 12(1) (2017) 1-15.
[62] C. Wang, D. Wu, P. Wang, Y. Ao, J. Hou, J. Qian, Effect of oxygen vacancy on enhanced photocatalytic activity of reduced ZnO nanorod arrays, Applied Surface Science 325 (2015) 112-116.
[63] K. Karuppasamy, I. Rabani, D. Vikraman, C. Bathula, J. Theerthagiri, R. Bose, C.-J. Yim, A. Kathalingam, Y.-S. Seo, H.-S. Kim, ZIF-8 templated assembly of La^{3+}-anchored ZnO distorted nano-hexagons as an efficient active photocatalyst for the detoxification of rhodamine B in water, Environmental Pollution 272 (2021) 116018.
[64] S. Payra, S. Challagulla, Y. Bobde, C. Chakraborty, B. Ghosh, S. Roy, Probing the photo- and electro-catalytic degradation mechanism of methylene blue dye over ZIF-derived ZnO, Journal of Hazardous Materials 373 (2019) 377-388.
[65] M. Hu, H. Lou, X. Yan, X. Hu, R. Feng, M. Zhou, In-situ fabrication of ZIF-8 decorated layered double oxides for adsorption and photocatalytic degradation of methylene blue, Microporous and Mesoporous Materials 271 (2018) 68-72.
[66] J. Mao, M. Ge, J. Huang, Y. Lai, C. Lin, K. Zhang, K. Meng, Y. Tang, Constructing multifunctional MOF@rGO hydro-/aerogels by the self-assembly process for customized water remediation, Journal of Materials Chemistry A 5(23) (2017) 11873-11881.
[67] J.T. Schneider, D.S. Firak, R.R. Ribeiro, P. Peralta-Zamora, Use of scavenger agents in heterogeneous photocatalysis: Truths, half-truths, and misinterpretations, Physical Chemistry Chemical Physics 22(27) (2020) 15723-15733.
[68] X.-Q. Liu, W.-J. Chen, H. Jiang, Facile synthesis of Ag/Ag_3PO_4/AMB composite with improved photocatalytic performance, Chemical Engineering Journal 308 (2017) 889-896.
[69] X. Rong, H. Chen, J. Rong, X. Zhang, J. Wei, S. Liu, X. Zhou, J. Xu, F. Qiu, Z. Wu, An all-solid-state Z-scheme $TiO_2/ZnFe_2O_4$ photocatalytic system for the N_2 photofixation enhancement, Chemical Engineering Journal 371 (2019) 286-293.
[70] Y.-J. Lee, J.-K. Kang, S.-J. Park, C.-G. Lee, J.-K. Moon, P.J. Alvarez, Photocatalytic degradation of neonicotinoid insecticides using sulfate-doped Ag_3PO_4 with enhanced visible light activity, Chemical Engineering Journal 402 (2020) 126183.
[71] J.-Y. Fu, L.-W. Chen, Y.-M. Dai, F.-Y. Liu, S.-T. Huang, C.-C. Chen, BiO_mF_n/BiO_xI_y/GO nanocomposites: Synthesis, characterization, and photocatalytic activity, Molecular Catalysis 455 (2018) 214-223.
[72] W. Cao, Y. An, L. Chen, Z. Qi, Visible-light-driven Ag_2MoO_4/Ag_3PO_4 composites with enhanced photocatalytic activity, Journal of Alloys and Compounds 701 (2017) 350-357.
[73] J. Buasakun, P. Srilaoong, G. Chaloeipote, R. Rattanakram, C. Wongchoosuk, T. Duangthongyou, Synergistic effect of ZnO/ZIF8 heterostructure material in photodegradation of methylene blue and volatile organic compounds with sensor operating at room temperature, Journal of Solid State Chemistry 289 (2020) 121494.

[74] Y. Cheng, X. Wang, Y. Mei, D. Wang, C. Ji, ZnCDs/ZnO@ZIF-8 Zeolite composites for the photocatalytic degradation of tetracycline, Catalysts 11(8) (2021) 934.